Abandoned farmland detection using single-year satellite images in Japan

Abandoned farmland detection using single-year satellite images in Japan

Yoshihiko Kobayashi[a] **and Tsuguki Kinoshita**[b,*]
[a]National Agriculture and Food Research Organization, Institute of Agricultural Machinery, Saitama City, Japan
[b]Ibaraki University, College of Agriculture, Ibaraki, Japan

Abstract. Mapping abandoned farmlands' location and spatial pattern is essential for rural planning. Monitoring small abandoned farmland based on dynamic farmland's phenology is challenging to due to conflict between spatial and temporal resolutions of conventional satellite missions. A unique approach that combines satellite constellation imagery with improved automatic radiometric normalization method for more temporally consistent reflectance were proposed. Applying it in Ami-town, Ibaraki Prefecture, Japan, abandoned farmlands were identified with 3-m resolution and a Kappa coefficient of 0.81 based on satellite constellation-based time-series data; however, the discrimination of the degree of abandonment was challenging. Unlike conventional abandoned farmland mapping approaches which targets spatially large area, our approach provides information at small, fragmented and abandoned farmland in East Asia that enables labor-saving monitoring of land use shifts. [DOI: 10.1117/1.JRS.17.014517]

Keywords: normalized difference vegetation index reconstruction; PlanetScope; phenological profile; satellite constellation; support vector machine.

Paper 220497G received Aug. 20, 2022; accepted for publication Feb. 13, 2023; published online Mar. 10, 2023.

1 Introduction

Farmland abandonment is a global socioeconomic phenomenon driving land-use change in various countries in the world.[1,2] However, abandoned farmland's extent and spatial patterns are not fully understood in most world regions,[3] which interrupts assessing the environmental and socioeconomic outcomes of farmland abandonment, such as food security or sustainable rural development.[3–5]

Developing procedures for mapping farmland abandonment using satellite images is required because satellite remote sensing is a promising tool for spatial mapping patterns of farmland abandonment. Existing studies have mainly adopted two different satellite images for mapping farmland abandonment. One is a satellite with middle-resolution and relatively low-observation frequency, such as Landsat TM/ETM+/OLI.[1,4,6–10] For example, Alcantara et al.[11] proposed mapping abandoned farmland at broad scales with coarse-resolution satellite Terra/Aqua MODIS imagery in Eastern Europe. The other is a satellite with coarser-resolution and high-observation frequency such as Terra/Aqua MODIS.[3,11] For example, Yin et al.[1] developed a method to detect the extent and the exact timing of agricultural land abandonment using Landsat TM/ETM+/OLI time series in Russia and Georgia.

These traditional satellites have some disadvantages for abandoned farmland mapping. Landsat TM/ETM+/OLI lacks enough observation frequency, and Terra/Aqua MODIS lacks enough spatial resolution for detailed farmland abandonment mapping based on the phenological profile in a single year. First, Terra/Aqua MODIS can capture phenological information by frequent observation. However, it is not suitable for small farmlands, which are more likely to be abandoned because they are difficult to use and require more labor than larger farmland. Secondly, Landsat TM/ETM+/OLI has a 30-m spatial resolution. It enables spatially detailed mapping; however, the revisit interval is 16 days. The observation frequency is not sufficient

*Address all correspondence to Tsuguki Kinoshita, tsuguki.kinoshita.00@vc.ibaraki.ac.jp

1931-3195/2023/$28.00

for intra-annual abandonment mapping using phenological profiles. Therefore, it is necessary to study the mapping method of abandoned farmland using satellite images with higher frequency and spatial resolution.

Satellite constellations can balance incompatible characteristics and spatial and temporal resolutions. A satellite constellation consists of many spacecraft working in concert to perform a specific function.[12] Therefore, the observation by satellite constellation can be treated as frequent observation by a single satellite. Each satellite is allowed to have a sensor with a high spatial resolution with a narrow field of view.

The "Planet"[13] is a commercial satellite operator founded in 2010 and offers constellations of small, standardized satellites[14] and it has begun to be used in the field of land use research in recent years. However, the satellite constellation is characterized by the fact that differences between sensors cause variations in reflectance over time because it is composed of multiple satellites. The cross-sensor inconsistency is a specific problem for satellite constellation because it consists of many nanosatellites with deliberately inexpensive sensor designs, such as nanosatellite Dove in PlanetScope launched by Planet.[15] Therefore, data consistency should be improved when PlanetScope images are utilized for abandonment detection. Houborg and McCabe[14] improved the quality of PlanetScope images based on a cubesat enabled spatio-temporal enhancement method. However, this method requires both Landsat and MODIS images. Another simple correcting method using only a single satellite constellation image is needed.

Furthermore, smoothing of time-series data is effective because it can reduce the temporary reduction of NDVI due to clouds that cannot be reduced by normalization. Various methods for reconstructing these NDVIs have mainly been applied to single satellites. Therefore, this study also investigated the applicability of existing NDVI reconstruction methods to satellite constellation images.

Also, current studies for farmland abandonment detection have used NDVI profiles derived from higher quality sensors, such as Terra/Aqua MODIS or Landsat TM/ETM+/OLI. The effectiveness of the phenology-based classification established for the higher quality sensors should be evaluated for the satellite constellation. Therefore, this study examines whether support vector machine (SVM), a classification method widely used in existing studies, can classify abandoned fields based on the differences in phenology profiles between abandoned and cultivated fields, as represented by normalized time series derived from satellite constellation images.

This research aimed to detect abandoned farmland with high resolution using single-year satellite data; our goal was to develop a method to improve PlanetScope reflectance consistency, reduce cloud effect from NDVI time series, and identify abandoned farmland based on NDVI time series and assess the following research questions.

1. How can the temporal consistency of satellite constellation time series be improved?
2. How can the phenological profile of abandoned and active farmland be reconstructed?
3. Is PlanetScope NDVI time series suited to distinguish farmland abandonment?

In addition, this study specifically aims to identify abandoned lands from 1 year of data, which will allow for early identification of abandoned lands based on a small amount of data.

2 Method

2.1 *Image Normalization*

2.1.1 *Automatic radiometric normalization*

We exploited automatic radiometric normalization.[16] This is one of the relative image correction methods. It has been used to preprocess abandoned farmland detection using multi-temporal satellite images.[9,10] Automatic radiometric normalization assumes a simple linear relationship among images across time calculated by stable features in the scene.[17]

The relative image correction cannot result in actual reflectance but generates temporally consistent reflectance time series. A relatively consistent reflectance is sufficient for abandoned farmland classification because it needs phenological profiles in a year. Canty et al.[16] established

this image correction method for Landsat TM images; moreover, they used it to normalize radiance. However, we applied this method to the PlanetScope surface reflectance product. This method is not limited to radiance, even if these correlate with time and can be applied to reflectance.

All scenes were normalized to a single reference image. We chose an image on October 2, 2018, as a reference image because the image has complete coverage of the study area and high clearness.

2.1.2 *Method improvement*

This study improved automatic radiometric normalization to remove water body pixels before selecting invariant pixels (see Appendix A). Water pixels have small correlations over time in PlanetScope images, disturbing normalization. The normalized difference water index (NDWI) can separate the water area from the land area, which is defined as follows:[18]

$$\mathrm{NDWI} = \frac{a_{\mathrm{green}} - a_{\mathrm{NIR}}}{a_{\mathrm{green}} + a_{\mathrm{NIR}}}, \tag{1}$$

where a_{green} is surface reflectance over green wavelength, and a_{NIR} is surface reflectance over near-infrared (NIR) wavelength. We set the threshold of NDWI to -0.2 and selected water pixels that have higher NDWI than the threshold (Fig. 1).

We implemented automatic radiometric normalization with the C language. We also used LibTIF 4.1.0, libgeotiff 1.6.0, Intel Math Kernel Library 2019.0-045 for processing in C.

2.1.3 *Validation*

We verified the effect of automatic radiometric normalization[16] by comparing reflectance time series before and after normalization at a reference site in the study area. We selected nine pixels

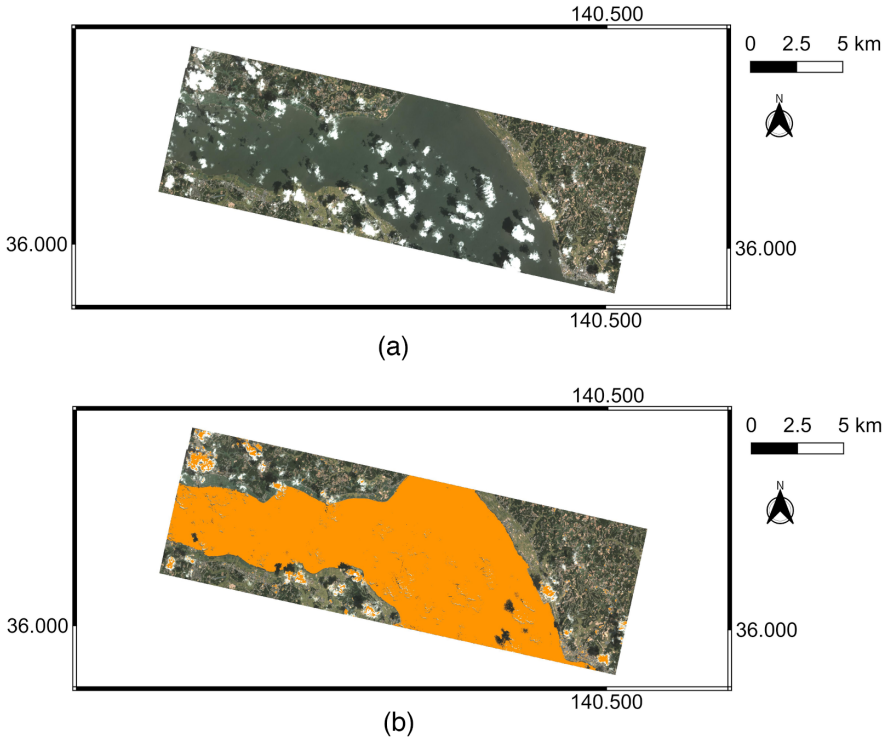

Fig. 1 Water detection using NDWI for PlanetScope image (ID: 20180822_005331_1042, RGB = Band 3, 2, 1); NDWI selects Lake Kasumigaura and a part of the clouds. (a) Without NDWI and (b) with NDWI > -0.2 (orange region).

as the reference site in a mixed forest dominated by cedar, evergreen coniferous trees with a uniform surface. We assumed that reflectance over the reference site is constant because leaves are green throughout the year.

2.2 *Intra-annual Phenological Profile*

2.2.1 *Normalized difference vegetation index*

The NDVI is one of the typical vegetation indexes widely used to detect vegetation phenology,[19,20] which strongly correlates with net primary productivity on the ground[21] or other physical properties of the vegetation canopy biomass.[22]

Abandoned and active farmlands have a different phenological profile,[23,24] such as seasonal changes in plant biomass. Temporal NDVI time series in unmanaged farmlands are smooth and bell-shaped, whereas managed farmlands have sudden changes.[3] Therefore, abandoned farmland can be separable by the NDVI time series. The NDVI is defined as follows:

$$\mathrm{NDVI} = \frac{a_{\mathrm{NIR}} - a_{\mathrm{red}}}{a_{\mathrm{NIR}} + a_{\mathrm{red}}}, \tag{2}$$

where a_{red} is surface reflectance over red wavelength, and a_{NIR} is surface reflectance over NIR wavelength.[22]

2.2.2 *Maximum value composite*

We smoothed the NDVI time series using the maximum value composite (MVC).[25] In MVC, each NDVI value is examined in the fixed interval. Only the highest value is retained for each pixel location; MVC minimizes cloud contamination and aerosol and water vapor effects.[25] We chose a 12-day interval for the NDVI compositing period because prior experiments have shown that 8-day and 16-day composites, such as those provided by MODIS, are problematic. Prior experiments have shown that 8-day NDVI composites and 16-day composites, such as those provided by MODIS, are problematic. In the 8-day composite, the cloud removal effect of multiple images is reduced due to the smaller number of images in the interval. Additionally, the 16-day composite did not capture enough land cover change in agricultural land due to the smaller number of smoothed data.

2.2.3 *Best index slope extraction*

Further, we smoothed the NDVI time series using the best index slope extraction (BISE).[26] The NDVI data contains some noise due to remnant cloud cover, water, snow, or shadow.[21] Both MVC and BISE utilize noise characteristics, decreasing the NDVI.[21,26] The BISE searches decreased NDVI by cloud in the prefixed sliding period based on percentage increase after NDVI decrease, which is applied to NDVI composite to reduce cloud effect that MVC could not remove. Here BISE was applied, as shown in Fig. 2. We used a 12-day compositing interval for MVC, resulting in an NDVI time series of 23 NDVI composites from 151 scenes in 81 days. We set the sliding period to three acquisitions and set the percentage increase to 30%. The false high,[26] which indicates a temporary and abnormal increase in NDVI, was defined as an increase in NDVI of 0.5 over 12 days and was removed from the NDVI time series and then interpolated by the previous and next NDVI values as in the BISE.

We implemented MVC and BISE with the C language. We also used LibTIF 4.1.0, libgeotiff 1.6.0, Intel Math Kernel Library 2019.0-045 for processing in C.

2.3 *Classification*

We performed the abandoned farmland classification using an SVM (scikit-learn 0.24.1). We performed a pixel-wise classification, and input data was NDVI time series in 23 dates. We used the hyperparameters shown in Table 1. Also, SVM classifies a single class and then

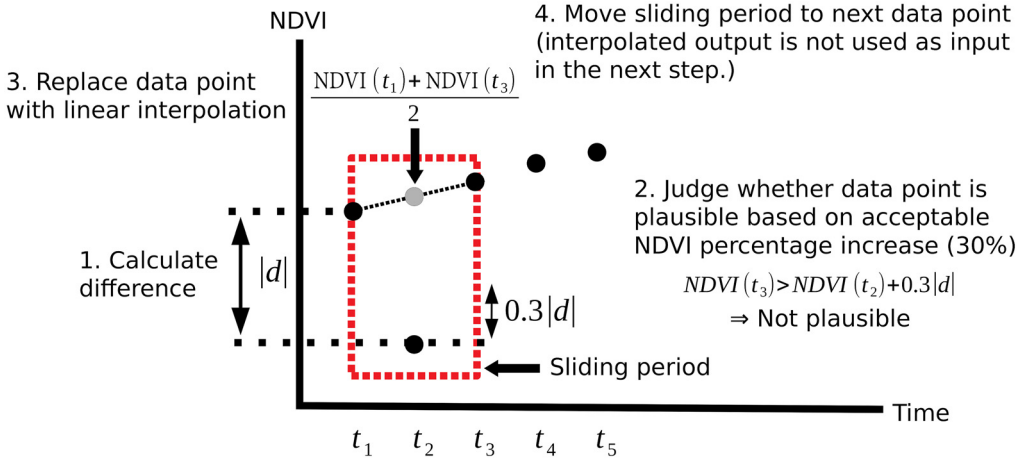

Fig. 2 Four steps for the BISE. NDVI: normalized difference vegetation index.

realizes multi-class classification by one-versus-one method. We used a five-fold grid search for model selection using scikit-learn 0.24.1. The kernel function is selected from radial basis function, polynomial, linear, and sigmoid. Gamma is selected from 1, 0.1, 0.01, and 0.001; C is selected from 1, 10, 100, and 1000. To shorten the computation time, the iteration limit was set to 10,000 when calculating the decision function of SVM. Even though the calculation results do not converge to the optimal global solution, there is no significant impact on the classification results because several iterations are ensured. Note that the land cover classes other than farmland (e.g., forests, urban areas, and water bodies) were excluded just before classification to focus on farmland classification[9,10] by clipping satellite images by farmland parcel polygons created based on a field survey. Therefore, pixels in nonagricultural land are used only for image normalization. The polygonization of the field survey result was conducted by QGIS Desktop 3.0.2. Clipping image by parcel polygons was conducted by GDAL 2.2.3.

Moreover, we set a negative buffer of parcel polygons to exclude border pixels from classification. The width of the buffering was determined as follows:

$$w = p * d * h = 3 * \sqrt{2} * \frac{1}{2} = 2.115, \tag{3}$$

Table 1 Parameters used for support vector classification class in scikit-learn for four-class classification.

Parameter	Value
cache_size	200
class_weight	None
decision_function_shape	“ovr”
Gamma	0.01 or 0.1
C	1 or 10
Kernel	“rbf”
max_iter	10000
random_state	None
Shrinking	True
Tol	0.001

where w is the width of buffering $[m]$, p is the pixel size $[m]$, d is the diagonal of square, and h is a half of the diagonal of pixel required for excluding border pixels. The above equation represents half the diagonal length of a PlanetScope pixel.

2.4 *Accuracy Assessment*

We used repeated stratified nested cross-validation for accuracy assessment.[27] We stratify the class labels and divide the dataset into five folds because 5- or 10-fold cross-validation is recommended.[28]

Each fold contains the same proportion of the five strata.[27] Polygons in reference data based on field surveys are randomly divided into five datasets. Random sampling based on polygons ensures randomness and independence of training and validation data; 80% and 20% of all polygons are used as training and validation data in each class, respectively. The validations were conducted five times for each dataset. This division of dataset is outer cross-validation in nested cross-validation for accuracy assessment.

Furthermore, five-fold grid search cross-validation for hyperparameter setting is conducted as inner cross-validation in nested cross-validation. We note that the inner cross-validation is performed on the basis of pixels. However, the outer cross-validation is performed based on polygons.

We made a confusion matrix[29] from five validation datasets. We sum up all five confusion matrices generated by validation dataset by five-fold cross-validation (outer cross-validation). We calculated the Kappa coefficient[29] for checking the classification results based on the confusion matrix. Moreover, we created a classification result map by combining five classified validation datasets in five-fold cross-validation and comparing them with ground truth. Figure 3 shows the flowchart of image processing in this study.

3 Data

3.1 *Study Area*

Our approach tested Ami-town, Ibaraki Prefecture, Japan (Fig. 4). The rate of abandoned farmland in Ami-town was 36.84%[30] in 2015, which is three times higher than the average rate in Japan (12.14%[30]). Ami-town is located on the Pacific side of Japan that has a temperate humid climate. The annual precipitation was 1021.5 mm in 2018 in Tsuchiura City, Ibaraki, Japan, near the study area.[31] Moreover, the annual mean temperature was 20.8°C in 2018 in Tsuchiura City.[31] In Ami-town, the paddy area occupies 730 ha. The upland field occupied 1120 ha in 2018.[32] Rice paddy occupies the largest area in farmlands, followed by green onion and Chinese cabbage;[33] there is little pasture in the study area. Because crop rotation is not practiced in the study area, abandonment of farmland is more likely to be a long-term cessation of farming than a fallow due to crop rotation.

3.2 *Satellite Image*

PlanetScope's satellite constellation consists of ∼130 satellites.[34] It can observe the Earth's entire land surface every day with ∼3.7 m ground sample distance.[34] Table 2 shows PlanetScope specification.

In this study, we used 151 four-band PlanetScope surface reflectance product[13] in 2018. The image is available for 81 days because adjacent scenes in a single day were used. PlanetScope images that meet the following conditions were downloaded from Ref. 13. First, the image covers 50% of the area represented by the following four points (Table 3). This polygon covers the area of Ami-town. Second, other conditions for downloading were set as follows (Table 4). Images with relatively low cloud cover (smaller than 30%) were used. Even if the cloud cover value is <30% in the PlanetScope metadata, some images covered by many clouds were excluded from the analysis by visual inspection.

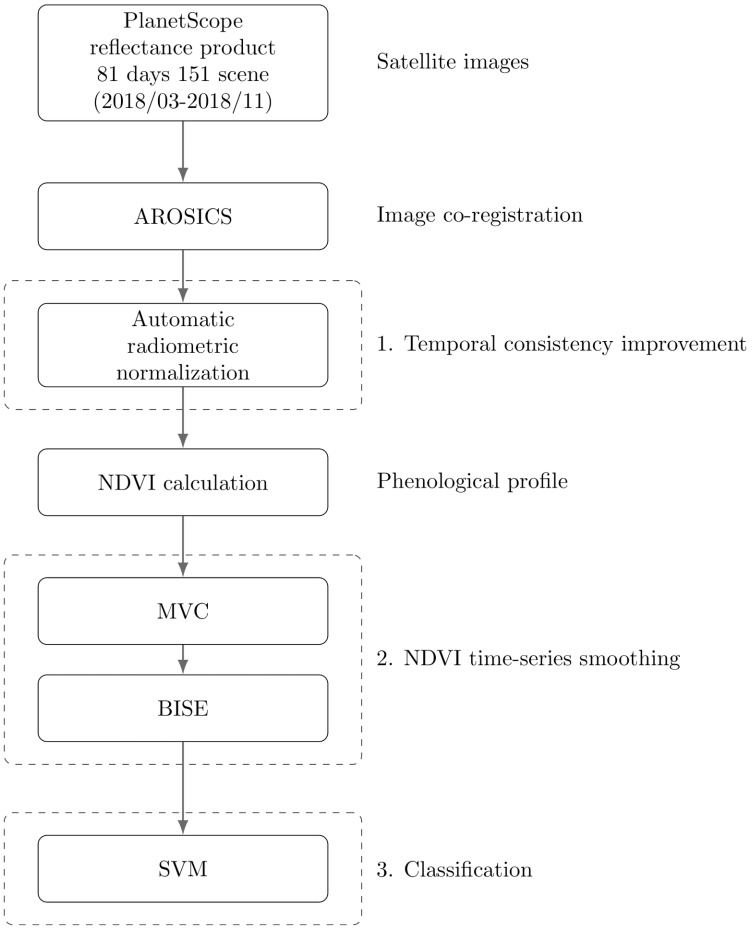

Fig. 3 The flowchart illustrates the main steps to correct satellite image, smooth NDVI time series, and classify farmland abandonment. AROSICS, automated and robust open-source image coregistration software for multisensor satellite data; MVC: maximum value composite; BISE: best index slope extraction; and SVM: support vector machine.

As for the PlanetScope instrument type, PS2 is used because the number of available images acquired by PS2 is bigger than those acquired by PS2.SD or PSB.SD and spectral wavelengths are not the same between them. The number of PlanetScope images used in this study was higher in March when the weather was clear and lower in June and July due to the rainy season (Fig. 5). We performed image coregistration using an automated and robust open-source image coregistration software[35] based on phase-only correlation.

3.3 *Class Setting and Field Data Acquisition*

This study defined abandoned farmland as without agricultural management, such as plowing or harvesting. We also tried to distinguish woody abandoned farmland and herbaceous abandoned farmland. The discrimination of the degree of abandonment is essential for the recultivation of abandoned farmland because pulling up trees by the root to convert abandoned farmland into active farmland takes much more effort than removing weeds.

The following farmlands were excluded from the class setting and analysis. First, abandoned farmland, which may have been mowed regularly, was excluded from the analysis because of the high heterogeneity within the class over time. Second, the tree nursery was excluded from the analysis because it is an uncommon agricultural land use. Third, the paddy field for lotus is omitted from the paddy class because it is an uncommon agricultural land use.

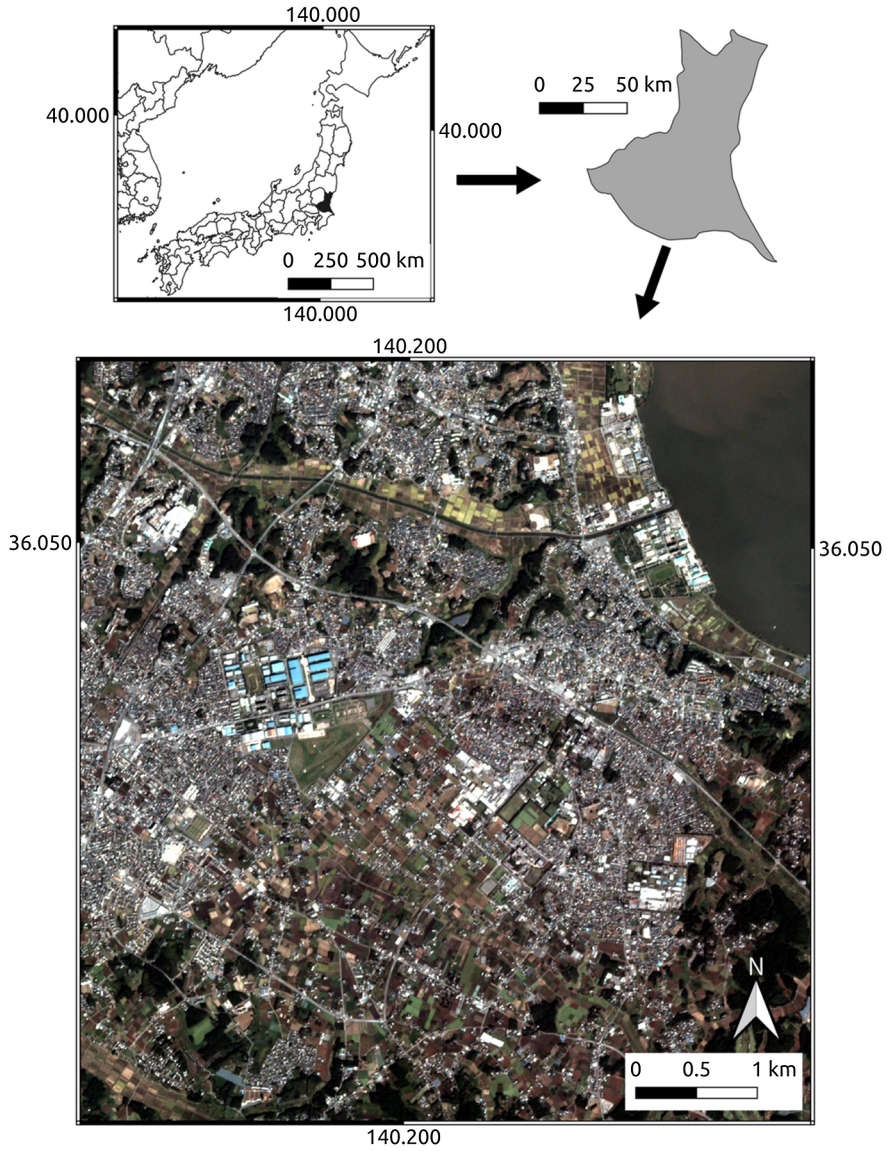

Fig. 4 Study area with PlanetScope image mosaic in October 2018 (20181001_005504_1035, 20181002_005438_1029, 20181007_005609_0f4e displayed in RGB = Band 3, 2, 1).

Table 2 Specifications of the PlanetScope satellite constellation based on Planet imagery product specifications.[34]

Mission characteristics	Sun-synchronous orbit
Orbit altitude (reference)	475 km (~98 deg inclination)
Sensor type	Four-band frame imager with a split-frame NIR[a] filter
Spectral bands	Blue: 455 to 515 nm
	Green: 500 to 590 nm
	Red: 590 to 670 nm
	NIRa: 780 to 860 nm
Ground sample distance (nadir)	3.7 m
Frame size	~24.6 km × 16.4 km
Revisit time	Daily at nadir

[a]near-infrared

Table 3 Area for retrieving PlanetScope images.

Longitude	Latitude
35.96825	140.15851
36.05556	140.15851
36.05556	140.28732
35.96825	140.28732

Table 4 Condition for retrieving PlanetScope images.

Parameter	Value
Source	4-band PlanetScope scene
Area coverage	51% to 100%
Cloud cover	0% to 30%
Instrument filter	PS2
Date	2018/03/01 to 2018/11/31
Radiometry	Surface reflectance
Rectification	Orthorectified

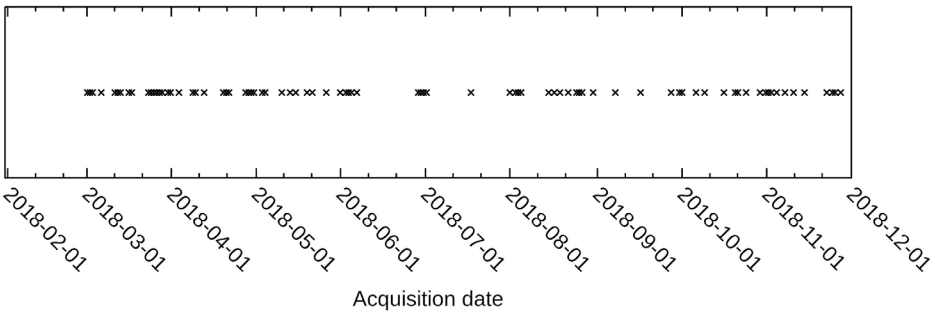

Fig. 5 PlanetScope images' acquisition date used for image composition from March 2018 to November 2018. Each point indicates a PlanetScope image acquisition.

As a result, four representative land cover/land use classes, abandoned (woody), abandoned (herbaceous), paddy, and upland fields were set and identified in this study (Table 5, Fig. 6).

For ground truth data collection, we visually assessed the cultivation status of farmlands on sites. We only surveyed municipalities and agricultural committees' administratively registered farmlands registered as "farmland;" we used the data available on Ref. 36. The field surveys were conducted in November 2018, December 2018, and March 2019. These results are used to analyze satellite data acquired from March to November 2018.

From the field survey results, uncertain and inappropriate data were removed, e.g. data of the land cover class label that could not be confidently determined due to inaccessibility or low visibility during the field survey were identified as complex data and removed from the analysis. Moreover, farmland with agricultural greenhouses was excluded from the analysis because the changes in land cover of agricultural greenhouses could not be observed. Tables 6 and 7 show the number and area of deletion. Figure 7 shows the parcel polygons of farmland for each class eventually used.

Table 5 Land use/land cover classes and their definitions.

No.	Class	Definition
1	Abandoned (woody)	Abandoned farmland where herbaceous and woody plants grow (at least one tree)
2	Abandoned (herbaceous)	Abandoned farmland where herbaceous plants grow (no trees)
3	Paddy	Paddy fields for rice
4	Upland field	Cropland for vegetables or crops other than rice

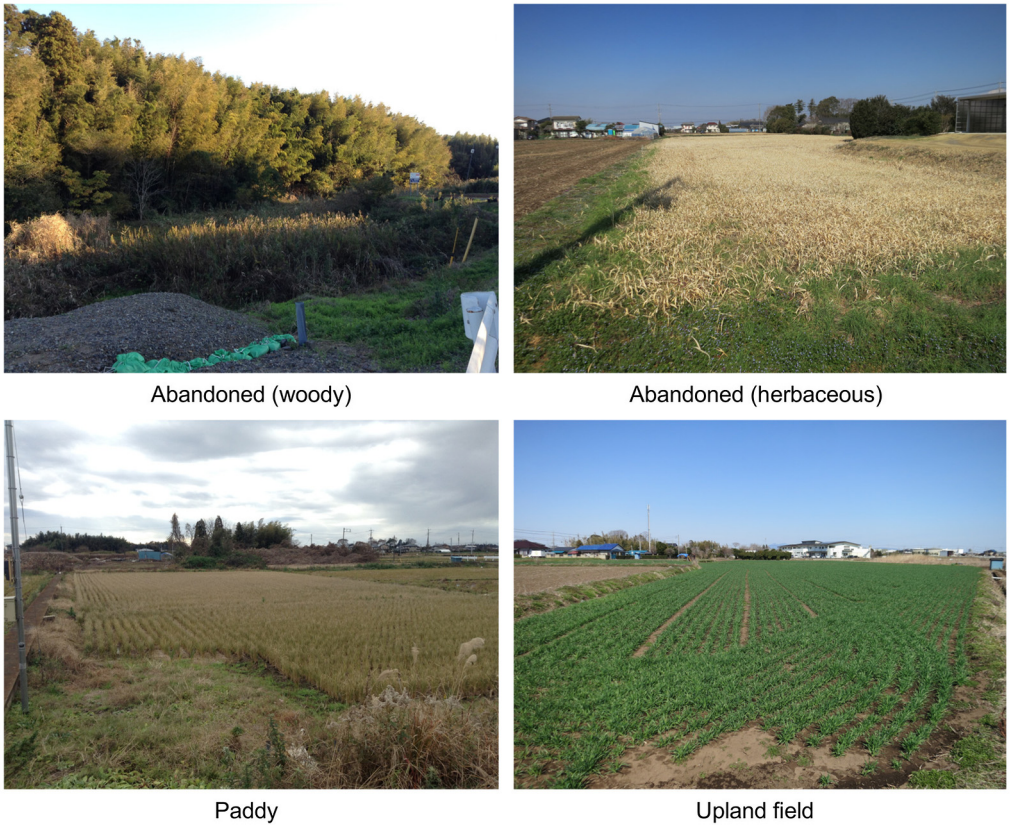

Fig. 6 Class setting.

Table 6 Number of polygons for each class before and after problematic polygon deletion.

Class	Original	After deletion	Rate of deletion
Abandoned (woody)	40	39	0.03
Abandoned (herbaceous)	139	132	0.05
Paddy	246	242	0.02
Upland filed	303	293	0.03

Table 7 Area of polygons for each class before and after problematic polygon deletion.

Class	Original	After deletion	Rate of deletion
Abandoned (woody)	6.1 ha	6.0 ha	0.02
Abandoned (herbaceous)	19.9 ha	19.1 ha	0.04
Paddy	81.3 ha	80.7 ha	0.01
Upland field	54.4 ha	52.8 ha	0.03

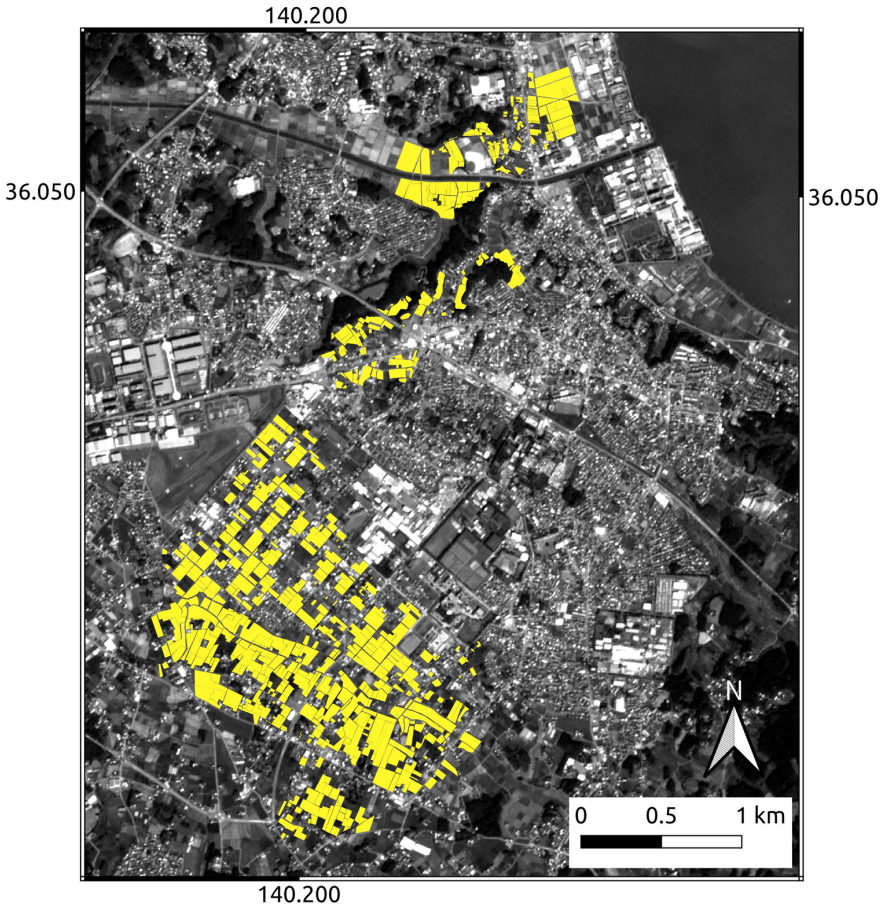

Fig. 7 Study area with PlanetScope image mosaic in October 2018 (20181001_005504_1035, 20181002_005438_1029 displayed as monochrome) with parcel polygon of paddy, upland field, abandoned (herbaceous), and abandoned (woody).

4 Results

4.1 *Validation of Normalization*

After normalization, the reflectance time series in all bands became closer to constant than before normalization at the reference site (Figs. 8 and 9). Normalization also brings NDVI closer to the constant (Figs. 10 and 11). To examine the intra-annual variability, we used the mean NDVI values for 9 pixels of adjacent evergreen coniferous forest. In the original PlanetScope image, the intra-annual means and standard deviations of pixel-averaged NDVI were 0.514 and 0.107. However, normalization reduced these to 0.627 and 0.045.

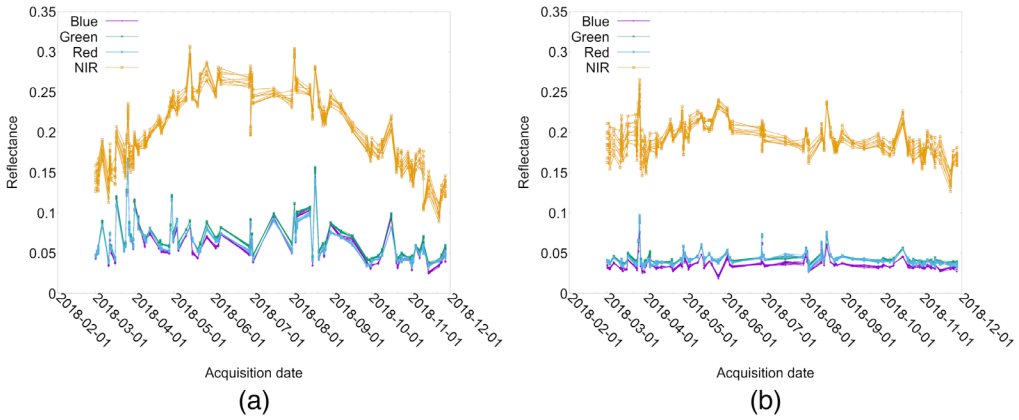

Fig. 8 Fluctuation of reflectance time series in 9 pixels (each line) in the forest before and after normalization. The horizontal axis is the acquisition date, and the vertical axis is reflectance. (a) original reflectance and (b) normalized reflectance.

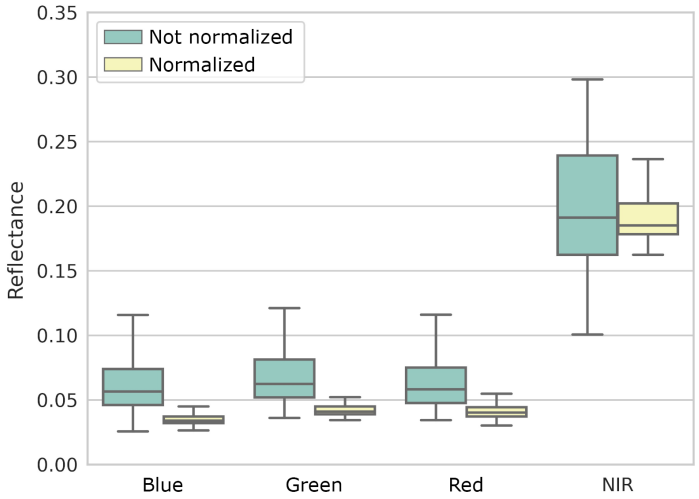

Fig. 9 Decreasing intra-annual fluctuation of reflectance in each band by normalization. The average reflectance of nine pixels in an evergreen coniferous forest (Table 8) is shown in the annual boxplots.

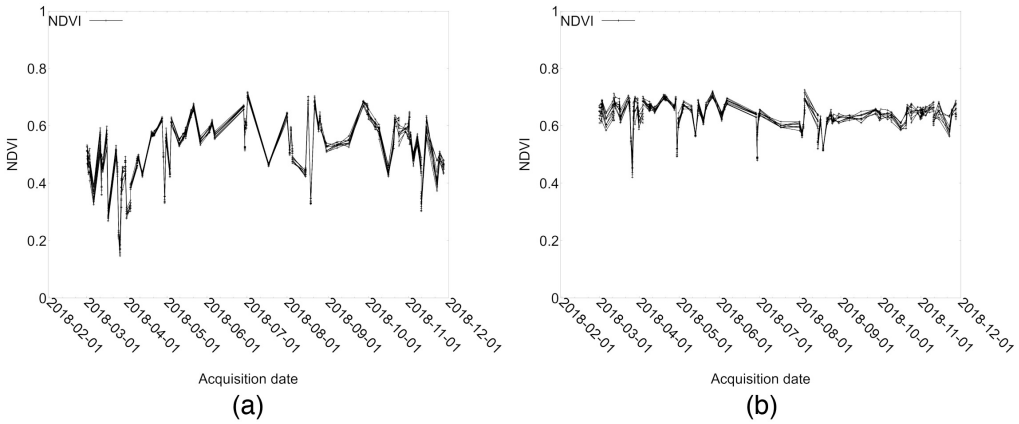

Fig. 10 Fluctuation of NDVI time series in 9 pixels (each line) in the forest before and after reflectance normalization. The horizontal axis is the acquisition date, and the vertical axis is NDVI. (a) Calculated by original reflectance and (b) calculated by normalized reflectance.

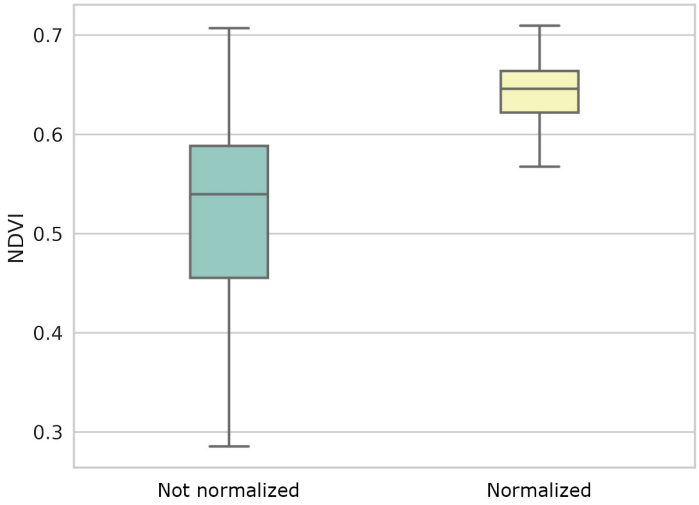

Fig. 11 Decreasing intra-annual fluctuation of NDVI by normalization. The average NDVI of nine pixels in an evergreen coniferous forest (Table 10) is shown in the annual boxplots.

Some data points still have low NDVI because of clouds and cloud shadows. These decreases can be removed by the smoothing process in the next step.

4.2 *Validation of Normalization Method Modification*

Original automatic radiometric normalization[16] sometimes does not work. For an image containing a body of water, the normalization result was implausible, as shown in Fig. 12. In this case, the slope and intercept of the linear equation applied to each band are shown in Table 8. The assumption for relative correction was that there would be a positive correlation between the reflectance of the two images. However, here the slope is close to zero. The flat slope indicates that the reflectance of the water area pixels in the PlanetScope image is close to uncorrelated in time and does not meet the assumption of relative correction.

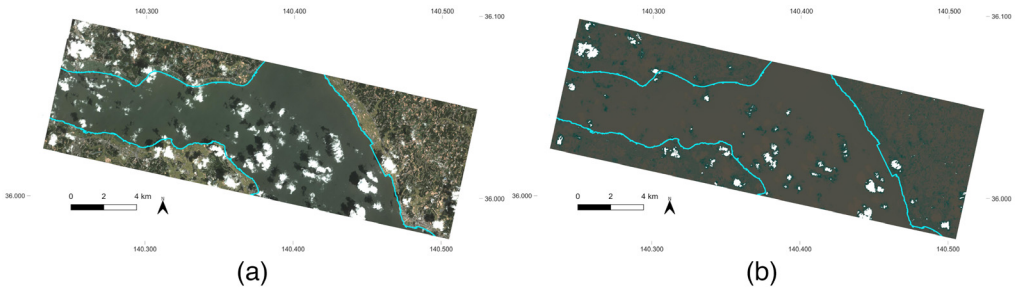

Fig. 12 Normalization failure when PlanetScope image over Lake Kasumigaura (ID: 20180822_005331_1042) is normalized (RGB = Band 3, 2, 1). (a) Original and (b) normalized.

Table 8 Normalization equation $y = ax + b$ for PlanetScope image containing water (ID: 20180822_005331_1042) when water pixels are not excluded.

Band	Slope	Intercept
Band 1	−0.013	0.0555
Band 2	−0.030	0.0673
Band 3	−0.24	0.0844
Band 4	0.55	0.0281

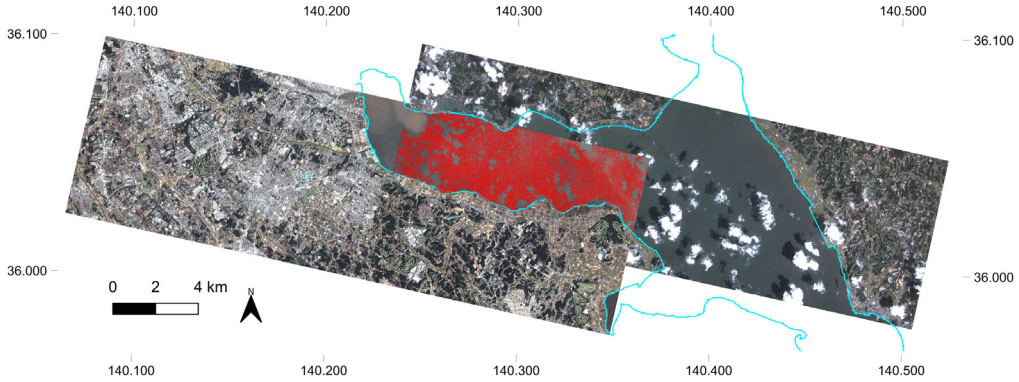

Fig. 13 Invariant pixels (red) used for estimating linear relationship between reference (left, ID: 20181002_005438_1029) and target (right, ID: 20180822_005331_1042) images in automatic radiometric normalization when water pixels are not excluded (RGB = Band 3, 2, 1).

The automatic radiometric normalization used in this study calculates the multivariate difference between the two images. It selects pixels with small values of the multivariate difference. These are called invariant pixels and estimate the linear relationship between the two images acquired on a different day. We checked the invariant pixels used to calculate the normalization equation in Table 8 and found that many water bodies were selected as invariant pixels (Fig. 13).

Figure 14 shows the scatter plot of the reflectance at the pixel used to calculate the normalization equation $y = ax + b$ for band 3 (red). The slope of the normalization equation is close to zero because the reflectance of the water area pixels is temporally uncorrelated.

Pixels with NDWI > -0.2 were determined as water body pixels and excluded from the normalization equation calculation. As a result, invariant pixels were selected, as shown in Fig. 15.

Here, the water area is no longer selected. Instead, the land area is selected as invariant pixels out of the overlapping area. Table 9 shows the slope and intercept of the normalized equation calculated after excluding the water area. The reflectances of the two images have a positive correlation, which is a reasonable result.

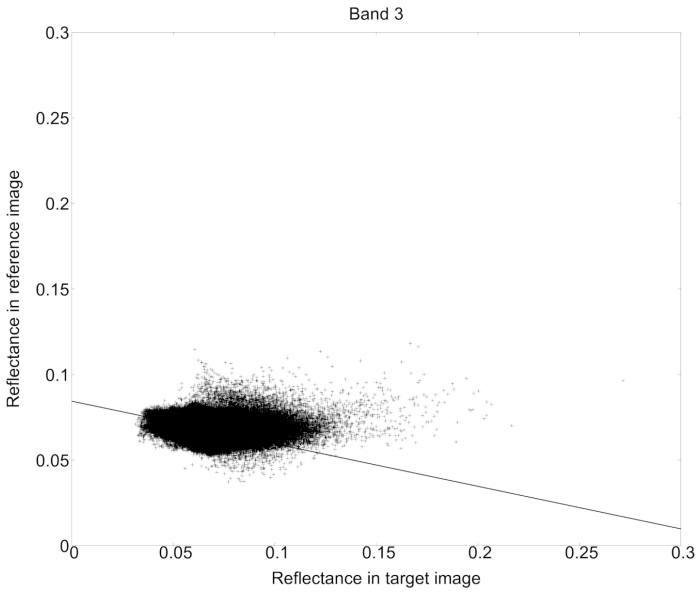

Fig. 14 Scatter plot of reflectance in band 3 (red) of target image (horizontal axis, ID: 20180822_005331_1042) and reference image (vertical axis, ID: 20181002_005438_1029) when water pixels are not excluded.

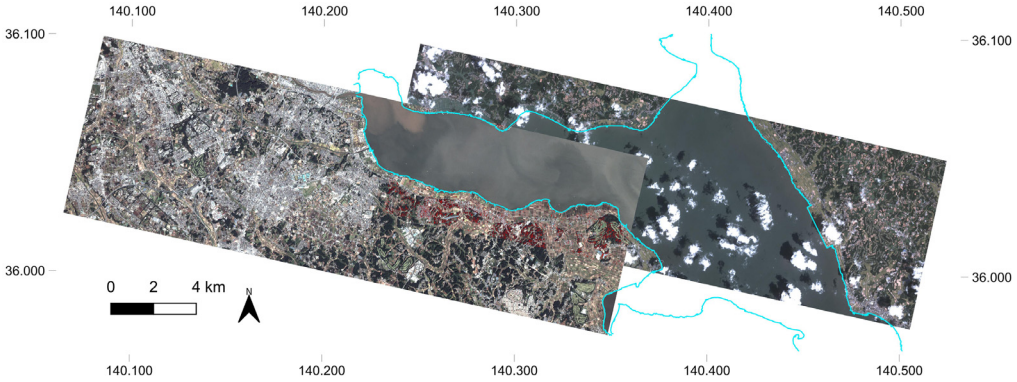

Fig. 15 Invariant pixels (red) used for estimating linear relationship between reference (left, ID: 20181002_005438_1029) and target (right, ID: 20180822_005331_1042) images in automatic radiometric normalization when NDWI is used (RGB = Band 3, 2, 1).

Table 9 Normalization equation $y = ax + b$ for PlanetScope image containing water (ID: 20180822_005331_1042) when water pixels are excluded.

Band	Slope	Intercept
Band 1	0.67	0.0088
Band 2	0.63	0.0111
Band 3	0.72	0.0079
Band 4	0.60	0.0407

Figure 16 shows the scatter plot of the reflectance at the pixel used to calculate the linear relationship for band 3 (red). When NDWI is used to exclude the water pixels from the normalization equation calculation, there is a positive correlation between the reflectance in the two images.

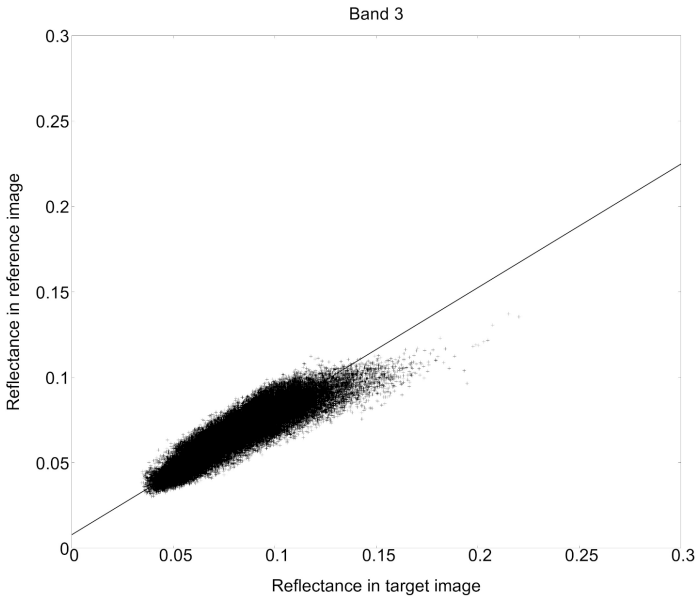

Fig. 16 Scatter plot of reflectance in band 3 (red) of target image (horizontal axis, ID: 20180822_005331_1042) and reference image (vertical axis, ID: 20181002_005438_1029) when water pixels are excluded.

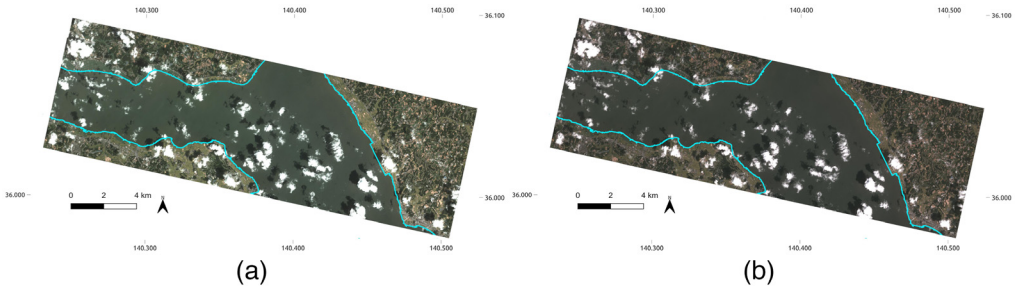

Fig. 17 Normalization success when PlanetScope image over Lake Kasumigaura (ID: 20180822_005331_1042) is normalized (RGB = Band 3, 2, 1) when water pixels are excluded. (a) Original and (b) normalized.

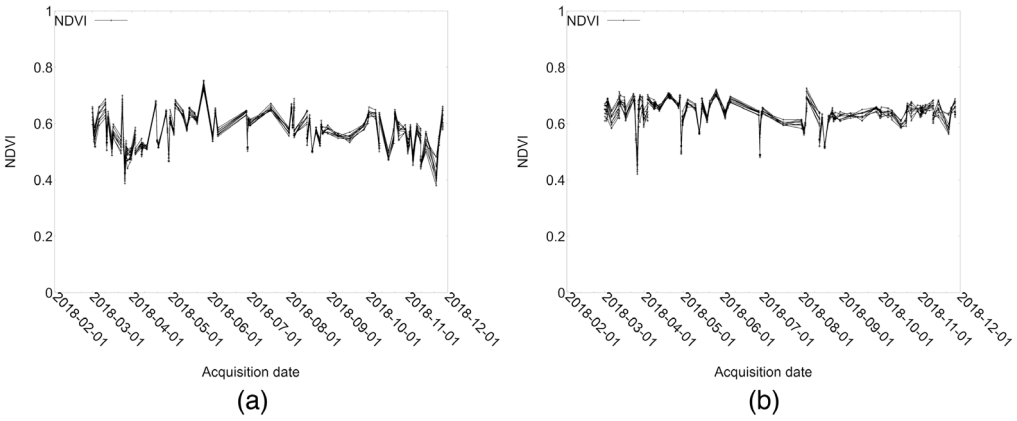

Fig. 18 Fluctuation of NDVI time series in 9 pixels (each line) in the forest with and without normalization method improvement. The horizontal axis is the acquisition date, and the vertical axis is reflectance. (a) Without water pixel exclusion (original method) and (b) with water pixel exclusion by NDWI (suggested in this study).

The normalization result image when using NDWI is shown in Fig. 17. Here, the normalization result image is reasonable compared to the original image before normalization (Fig. 12).

Figures 18 and 19 shows the effect of water exclusion by NDWI; NDVI becomes more consistent over time, and the fluctuation of NDVI to upper value rarely occurs. Noise that expresses low NDVI in time series can be removed by capturing the upper envelope of the NDVI time series by MVC and BISE.

4.3 *Effect of NDVI Time Series Reconstruction and Phenological Profiles in Each Class*

The NDVI time series were generated from 151 normalized reflectance products; MVC and BISE were applied to produce smoothed 12-day interval NDVI time series for 23 dates. Figure 20 shows phenological profiles in 2018 from different land cover types. Abandoned farmland [abandoned (herbaceous) and abandoned (woody)] and active farmland (paddy and upland field) show contrasting NDVI seasonal changes. Especially in paddy fields, NDVI is small before planting (from April to May) and after harvest (from October to November), indicating a decrease in biomass according to tilling of the ground surface prior to transplanting seedlings and removal plant materials from the field for harvesting. In addition, the considerable seasonal variation of NDVI was shown in paddy and upland fields.

However, abandoned (herbaceous) and abandoned (woody) showed a slight seasonal variation of NDVI. In particular, seasonal change in NDVI in abandoned (woody) is slight. The NDVI

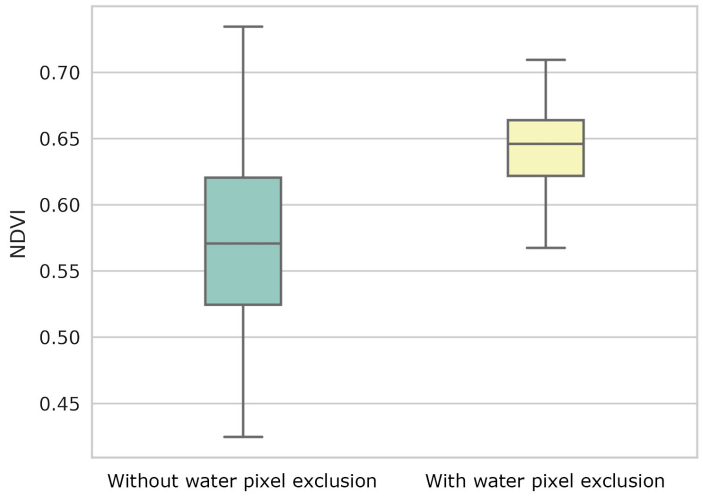

Fig. 19 Decreasing intra-annual fluctuation of NDVI by improvement of automatic radiometric normalization. The average NDVI of nine pixels in an evergreen coniferous forest (Table 18) is shown in the annual boxplots.

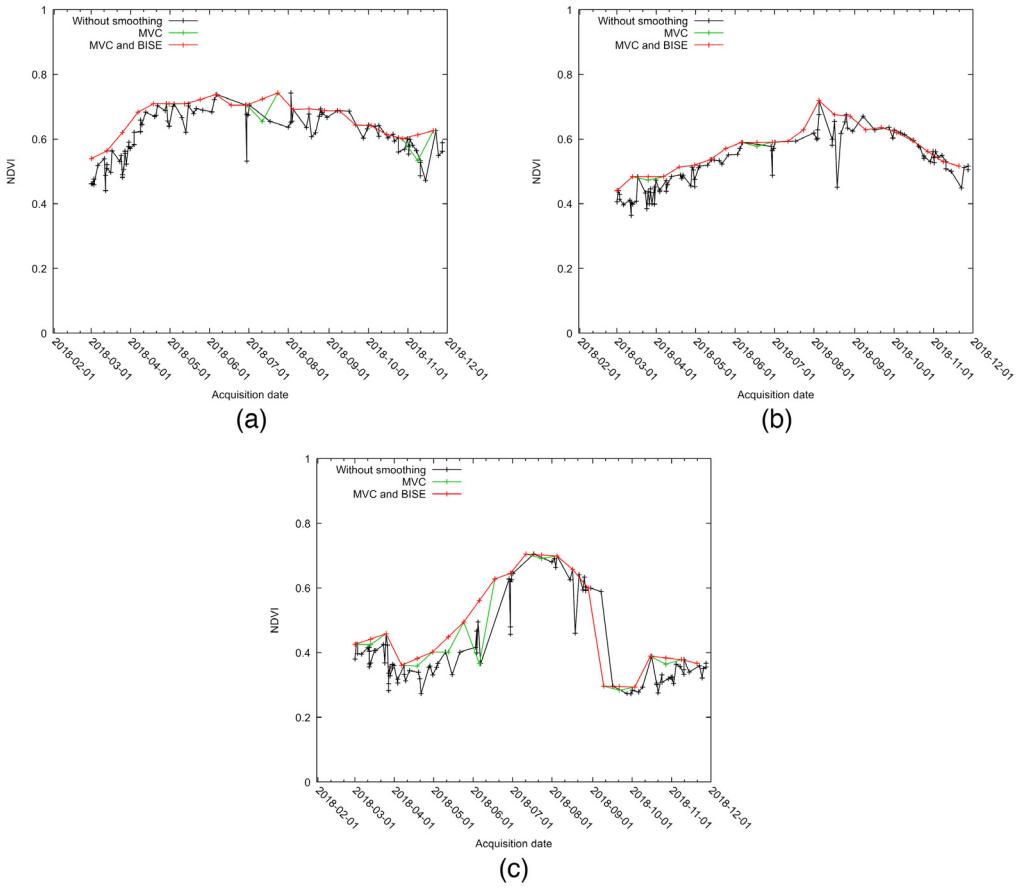

Fig. 20 NDVI time series in abandoned (woody), abandoned (herbaceous), paddy (X: 23 NDVI composite images from 2018/03/02 to 2018/11/21 during 12 days, Y: NDVI). MVC: maximum value composite and BISE: best index slope extraction. (a) Abandoned (woody), (b) abandoned (herbaceous), and (c) paddy.

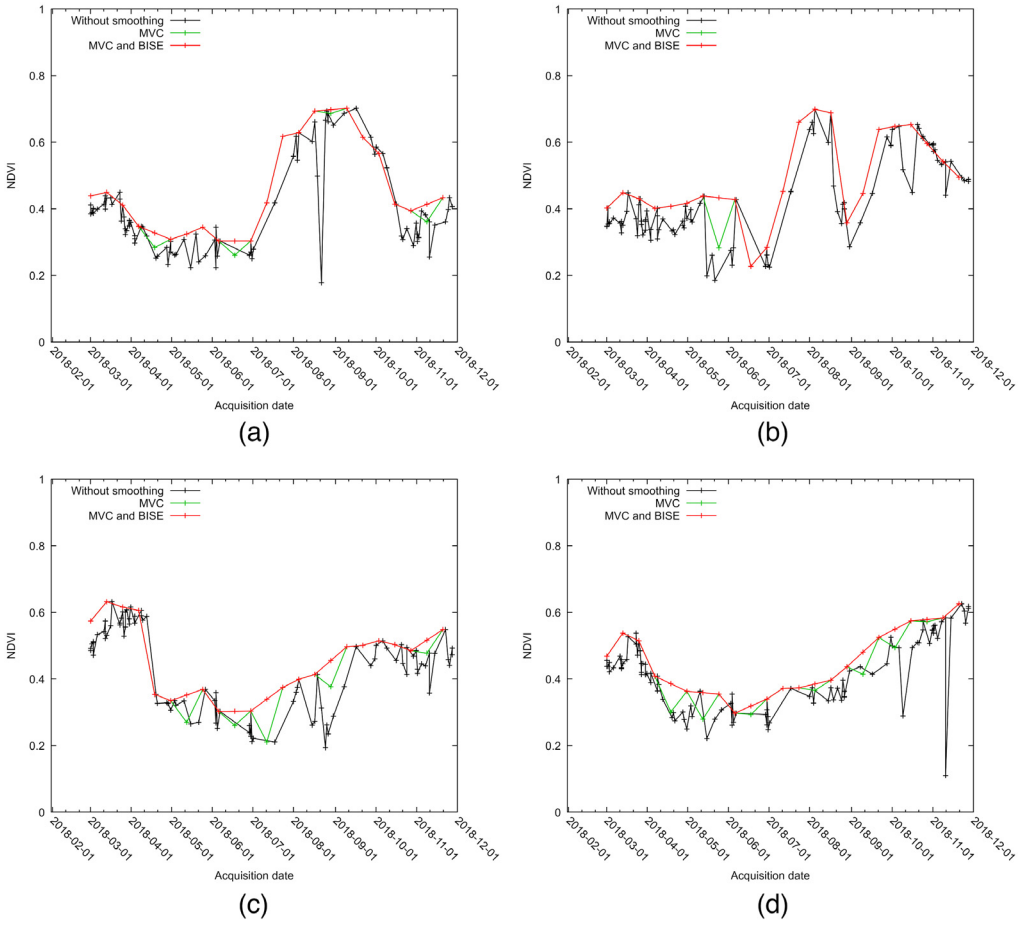

Fig. 21 NDVI time series (recorded crop type) at the upland field. The horizontal axis shows 23 dates every 12 days from 2018/03/02 to 2018/11/21, and the vertical axis shows NDVI after composite and smoothing. (a) Peanuts, (b) buckwheat, (c) canola flower, and (d) green onion.

time series in the upland field class differs depending on crops grown in each parcel in contrast to the paddy class, where only rice is grown.

Figure 21 shows the NDVI time series for a single pixel for some fields since it was not recorded for all crops in a field. Figures 21(a) and 21(b) show the NDVI time series of peanuts and buckwheat, respectively, with the growth and harvest of the crops. Figure 21(c) shows the NDVI time series of canola, which was harvested in spring. Figure 21(d) shows the NDVI time series of green onions, a winter crop; the NDVI increases in winter. Overall, the upland field class shows various NDVI time series.

4.4 *Classification Results and Accuracy*

The Kappa coefficient's average and standard deviation for five validation datasets are 0.814 ± 0.014. Table 10 is the confusion matrix of the map of abandoned or active farmland using the SVM. The number in each cell of the confusion matrix represents the number of pixels. The rows show the ground truth data, and the columns show the classification classes resulting from satellite data. The Kappa coefficient is 0.814.

In contrast, the Kappa coefficient's average and standard deviation for five validation datasets are 0.802 ± 0.017 when water pixel exclusion is not performed. Table 11 is the confusion matrix of the map of abandoned or active farmland using the SVM. The Kappa coefficient is 0.802.

Figure 22 shows the result of abandonment mapping. The field survey result is also displayed next to the classification result. The classification result image is generated as the sum of five classified maps of five validation datasets in cross-validation. As shown in the confusion matrix,

Table 10 Confusion matrix of active and abandoned farmland map using the SVM classifier when NDWI time series for 2018 is used as input data.

		Classification result			
		Abandoned (woody)	Abandoned (herbaceous)	Paddy	Upland field
Ground truth	Abandoned (woody)	1758	4364	124	427
	Abandoned (herbaceous)	1803	14702	1672	3065
	Paddy	15	1296	86145	2111
	Upland field	297	2168	2643	53524

Note: This result is based on the normalization method where water pixel exclusion by NDWI is performed.

Table 11 Confusion matrix of active and abandoned farmland map using the SVM classifier when NDWI time series for 2018 is used as an input data and water pixel exclusion by NDWI is not performed in normalization.

		Classification result			
		Abandoned (woody)	Abandoned (herbaceous)	Paddy	Upland field
Ground truth	Abandoned (woody)	1974	4048	128	523
	Abandoned (herbaceous)	1840	14093	1838	3469
	Paddy	20	1431	85383	2733
	Upland field	284	2029	2917	53402

Note: The number in each cell of the confusion matrix represents the number of pixels. The rows show the ground truth data, and the columns show the classification classes resulting from the satellite data.

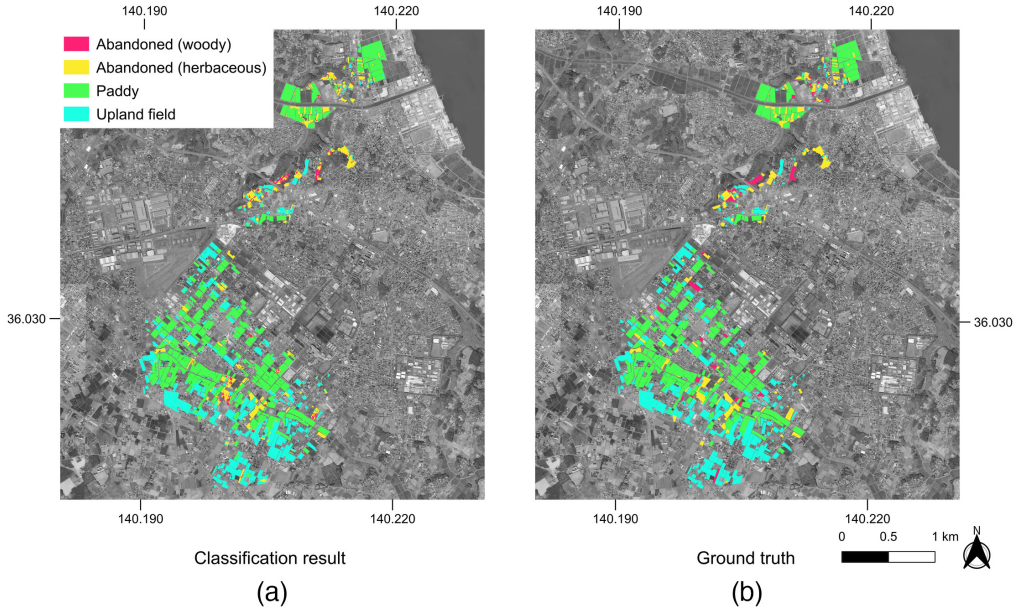

Fig. 22 Classification result of four classes using SVM classification (a) and ground truth (b) overlaid on an aerial photograph from the Geospatial Information Authority of Japan.

the classification results mostly agree with the field survey results, except for the abandoned (woody) class.

5 Discussion

5.1 *Our Method and Advantages*

We suggested several procedures for mapping abandoned farmland timely at high spatial resolution using single-year satellite constellation images. Our method is helpful to cope with the lack of reliable annual field surveys of abandonment.

The advantage of our method arises from the following aspects. First, the NDVI time series corrected by automatic radiometric normalization enables us to grasp intra-annual vegetation dynamics. We set a single reference image, and then, based on the reference image, all images were normalized. It reduced the temporal inconsistency of reflectance, which comes from the difference in sensors and atmospheric conditions. Automatic radiometric normalization has been used for normalizing single satellite images such as Landsat TM, Landsat ETM+, and SPOT HRV images.[16] However, our study has shown that this method can be applied to satellite constellation images, consisting of many similar satellites with different sensor conditions.

Second, we have shown that these simple established NDVI smoothing methods (MVC and BISE) are sufficient for phenology-based abandonment mapping. In other words, the combination of MVC and BISE can generate smoother NDVI time series from both clear and cloudy images. Further, we also showed that it is effective for PlanetScope satellite constellation images.

Third, the uses of satellite constellations are reasonable when mapping at a local scale with high spatial resolution. PlanetScope has a high temporal resolution to detect abandoned farmland from active farmland based on the fluctuation of NDVI by rapid land cover change. It can indicate potentially abandoned farmland using SVM with high accuracy. Therefore, PlanetScope is a possible new satellite image source in addition to Terra/Aqua MODIS[3,11] and Landsat TM/ETM+/OLI[1,6,8] for detecting abandoned farmland in existing studies.

5.2 *Interpretation of Results*

As shown in Figs. 8–11, the automatic radiometric normalization method leads to more consistent reflectance and NDVI. That indicates normalization improved time series inconsistencies according to atmospheric conditions and sensors. These are useful for observing the phenology of agricultural land, as shown in Figs. 20 and 21. The linear relationship equation of the two images can include the atmospheric conditions and the differences between satellites in the satellite constellation together, which is appropriate for the correction of satellite constellation images.

In addition, the water body removal process proposed in this study improves the automatic radiometric normalization method: numerous water body pixels (Fig. 13), which are selected based on small changes between two-time points, do not satisfy the assumption of positive correlation of reflectance between two-time points (Fig. 14, Table 8) and produce erroneous normalization results (Fig. 12). By excluding the water pixels from the normalization equation, only the land pixels are used in the normalization equation calculation (Fig. 15); the reflectance between the two-time points is positively correlated (Fig. 16 and Table 9), and the resulting normalization result is valid (Fig. 17).

We applied MVC and BISE, a smoothing technique that takes advantage of the NDVI property of being degraded by clouds, to reduce effect of cloud contamination to the reflectance after normalization. This is because the growing season of summer crops such as rice, soybeans, eggplant, and corn in Japan is close to the rainy season (June to July in the study area). Cloud contamination is a bigger problem than other regions. Figures 20 and 21 show the results of the application of MVC and BISE, where the successive application of different smoothing methods produces a more empirically valid NDVI time series, representing the small intra-annual biomass variability in the abandoned farmland.

The outcome of our experiment to discriminate abandoned farmland from active farmland showed a high Kappa coefficient of 0.814. However, based on the confusion matrix (Table 10), the producer's abandoned (woody) accuracy is 26%. Our result shows the difficulty in dividing abandoned farmland based on the degree of abandonment. That may be because that we set the class definition of abandoned (woody) as "farmland with at least one tree." However, when abandoned (woody) and abandoned (herbaceous) in the confusion matrix (Table 10) are integrated as "abandoned" class as postclassification processing, the Kappa coefficient increases from 0.814 to 0.870 (this 3×3 confusion matrix is not shown in this paper). Therefore, the objective of discrimination of abandoned farmland from active farmland succeeded.

5.3 *Uncertainty and Limitations*

Our method has some concerns. Some abandoned farmland is not used for agriculture but is managed. Farmers no longer cultivate the farmland, but they sometimes cut off the weeds in the farmland. However, our study focused on abandoned farmland with constant weeds, so we excluded these managed, unused farmlands from the analysis. Therefore, our maps based on field surveys may underestimate or overestimate the real abandonment.

Moreover, images from March to November are used. However, NDVI of winter crops increases toward winter, so images from the entire year are necessary for further crop type classification.

Our method supposes the homogeneity of vegetation growth patterns. If that area has a uniform vegetation type or crop calendar, the phenological profile detected from the NDVI time series may be the same. Therefore, this method can be scaled up to larger areas than the study area. However, it is not easy to apply national-scale or world-scale mapping.

In addition, the relative image correction requires that all images are overlapped, which makes applying this method to a broader region than the reference image for normalization difficult. The method proposed in this study has been tested only in a limited area. Therefore, the discussion on image correction and NDVI time series smoothing for satellite constellation images should be tested in other regions or other years' data.

6 Conclusions

PlanetScope satellite constellation archives contribute remarkable opportunities for understanding land use by time series of high spatial resolution of 4 m and nearly daily high temporal resolution images. Our study focused on the effectiveness of PlanetScope images in a single year to generate accurate farmland abandonment mapping in a temperate humid climate.

We developed a method for mapping agricultural abandonment by combining relative image correction, MVC/BISE, and SVM classification methods using NDVI time series. We tested the method in a study area where rice and other vegetable farming are performed.

This method visualized the vegetation dynamics in a year. It detected farmland abandonment with a Kappa coefficient of 0.814 ± 0.014. The results showed that satellite constellation was applicable when satellite images were masked using farmland parcel polygons.

Our study showed that the established relative image correction method called automatic radiometric normalization could mitigate not only atmospheric conditions but also the difference between satellites in satellite constellation, leading to consistent NDVI time series. In addition, we proposed not to use the pixels of the water region in the selection method of invariant pixels in automatic radiometric normalization. The slope of the normalization equation, which ranged from -0.013 to 0.55 when using pixels in the water area, improved to between 0.60 and 0.72 when not using pixels in the water area. This showed that the positive correlation between the reflectance of the two images was captured, leading to a more reasonable normalization result. To evaluate this improved normalization method, we used the average NDVI in nine adjacent evergreen coniferous forest pixels; the annual standard deviation of NDVI decreased from 0.107 to 0.045, suggesting improved image consistency.

Periodical abandoned farmland mapping with high spatial resolution produces a broad perspective on farmland abandonment. Our study contributes to mapping abandonment without a minor effort for field surveys.

7 Appendix A: Automatic Radiometric Normalization

We exploited automatic radiometric normalization.[16] This section introduces this method by selecting unchanged pixels using multivariate alteration detection (MAD).[37] The MAD method automatically detects the stable pixels from the two images. The selected pixels have relatively similar reflectance between two images and are called invariant pixels. To be specific, MAD has three steps as follows.

First, MAD calculates linear combinations of the original bands; it selects linear combination coefficients based on canonical correlation analysis to maximize multivariate differences between reference and the target image.[9] The linear combination of all bands in an image is called a canonical variate. Canonical correlation analysis maximizes the variance between linear combinations of each band in two images, and it results in maximizing change information over two images. It is suitable for selecting invariant pixels.[16]

We set a rule for and changed the signs of all eigenvectors because they are ambiguous, thereby influencing the result of canonical correlation analysis. First, an all-ones column vector is set as the reference vector. Second, the inner product between the reference vector and the target eigenvector is calculated. If it is negative, the sign of all eigenvectors is inversed. For example, original eigenvector $x = (-1, -2, -3, -4)$ is equal to eigenvector $x' = (1, 2, 3, 4)$. We set all-ones column vector $a = (1, 1, 1, 1)$. Furthermore, the inner product $a \cdot x$ becomes -10. Therefore, a sign of the original eigenvector is inversed, and a new eigenvector $x' = (1, 2, 3, 4)$ is used for the following calculation.

Second, the canonical variate in the target image is subtracted from the canonical variate in the reference image. It means the multivariate difference of two multispectral images.[9]

Third, pixels with a slight multivariate difference are selected as unchanged pixels between two dates. These pixels are unchanged features for normalization. The detection of the invariant pixel is performed based on the threshold as the index of change. The threshold is automatically defined by chi-square distribution with approximately N degrees of freedom (N is the number of channels).[16] Therefore, this method does not support arbitrarily choosing parameters.[9] More specifically, we can choose threshold $t = \chi^2_{N,P}$ where P is the probability of observing that value of t or lower. We set degrees of freedom $N = 4$, which equal the band number of PlanetScope PS2 product, and a lower cumulative probability $P = 0.01$ following Canty et al..[16] Then, the threshold $t = \chi^2_{N=4,P=0.01}$ is about 0.297. Therefore, if the change index between two images is less than 0.297, the pixel is selected as an unchanged pixel. A linear relationship between reflectance in the reference and target images is calculated using regression analysis from unchanged pixels for each band. Following Canty et al.,[16] we used orthogonal regression because reference image of normalization is arbitrary, so error in both x, y should be allowed. This method automatically selects the point with the least change for normalization from the two images. The normalization results are reproducible because the user does not need to select the reference point.[16]

Note that automatic radiometric normalization uses all four bands (visible and NIR) in the PlanetScope image for selecting invariant pixels. Further, the classification described in the next section uses only red and NIR bands because the classification is based on NDVI. In other words, blue and green bands were used only for the normalization. Red and NIR bands were used for automatic radiometric normalization and classification based on NDVI.

Although the reference and target images for normalization in this study were both 4-band PlanetScope images, they do not necessarily have to be the same type of image and can be applied even if the number of bands is different.[16] This also makes it possible to use satellite images of higher quality as a reference for normalization, which is highly versatile.

Acknowledgments

This work was supported by the JSPS KAKENHI (Grant No. JP19K06307). The authors have no conflicts of interest to declare.

Code, Data, and Materials Availability

The data that support the findings of this study are available from the corresponding author, T.K., upon reasonable request.

References

1. H. Yin et al., "Mapping agricultural land abandonment from spatial and temporal segmentation of Landsat time series," *Remote Sens. Environ.* **210**, 12–24 (2018).
2. D. Xu et al., "Labor migration and farmland abandonment in rural China: empirical results and policy implications," *J. Environ. Manage.* **232**, 738–750 (2019).
3. S. Estel et al., "Mapping farmland abandonment and recultivation across Europe using MODIS NDVI time series," *Remote Sens. Environ.* **163**, 312–325 (2015).
4. A. V. Prishchepov et al., "The effect of Landsat ETM/ETM+ image acquisition dates on the detection of agricultural land abandonment in Eastern Europe," *Remote Sens. Environ.* **126**, 195–209 (2012).
5. H. Xie, P. Wang, and G. Yao, "Exploring the dynamic mechanisms of farmland abandonment based on a spatially explicit economic model for environmental sustainability: a case study in Jiangxi Province, China," *Sustainability* **6**(3), 1260–1282 (2014).
6. A. Dara et al., "Mapping the timing of cropland abandonment and recultivation in northern Kazakhstan using annual Landsat time series," *Remote Sens. Environ.* **213**, 49–60 (2018).
7. H. Yin et al., "Monitoring cropland abandonment with Landsat time series," *Remote Sens. Environ.* **246**, 111873 (2020).
8. F. Löw et al., "Mapping abandoned agricultural land in Kyzyl-Orda, Kazakhstan using satellite remote sensing," *Appl. Geogr.* **62**, 377–390 (2015).
9. F. D. W. Witmer, "Detecting war-induced abandoned agricultural land in northeast Bosnia using multispectral, multitemporal Landsat TM imagery," *Int. J. Remote Sens.* **29**(13), 3805–3831 (2008).
10. N. M. Yusoff and F. M. Muharam, "The use of multi-temporal landsat imageries in detecting seasonal crop abandonment," *Remote Sens.* **7**(9), 11974–11991 (2015).
11. C. Alcantara et al., "Mapping abandoned agriculture with multi-temporal MODIS satellite data," *Remote Sens. Environ.* **124**, 334–347 (2012).
12. C. Pardini and L. Anselmo, "Environmental sustainability of large satellite constellations in low earth orbit," *Acta Astronaut.* **170**, 27–36 (2020).
13. Planet Team, "Planet application program interface: In space for life on earth. San Francisco, CA" (2017). https://api.planet.com
14. R. Houborg and M. F. McCabe, "A cubesat enabled spatio-temporal enhancement method (CESTEM) utilizing planet, LandSat and MODIS data," *Remote Sens. Environ.* **209**, 211–226 (2018).
15. R. Houborg and M. F. McCabe, "High-resolution NDVI from planet's constellation of earth observing nano-satellites: a new data source for precision agriculture," *Remote Sens.* **8**(9), 768 (2016).
16. M. J. Canty, A. A. Nielsen, and M. Schmidt, "Automatic radiometric normalization of multitemporal satellite imagery," *Remote Sens. Environ.* **91**(3–4), 441–451 (2004).
17. C. Song et al., "Classification and change detection using Landsat TM data: when and how to correct atmospheric effects?" *Remote Sens. Environ.* **75**(2), 230–244 (2001).
18. H. Xu, "Modification of normalized difference water index (NDWI) to enhance open water features in remotely sensed imagery," *Int. J. Remote Sens.* **27**(14), 3025–3033 (2006).
19. L. Zeng et al., "A review of vegetation phenological metrics extraction using time-series, multispectral satellite data," *Remote Sens. Environ.* **237**, 111511 (2020).
20. X. Zhang et al., "Monitoring vegetation phenology using MODIS," *Remote Sens. Environ.* **84**(3), 471–475 (2003).
21. N. Pettorelli et al., "Using the satellite-derived NDVI to assess ecological responses to environmental change," *Trends Ecol. Evol.* **20**(9), 503–510 (2005).
22. T. N. Carlson and D. A. Ripley, "On the relation between NDVI, fractional vegetation cover, and leaf area index," *Remote Sens. Environ.* **62**(3), 241–252 (1997).
23. M. L. Clark et al., "A scalable approach to mapping annual land cover at 250 m using MODIS time series data: a case study in the Dry Chaco ecoregion of South America," *Remote Sens. Environ.* **114**(11), 2816–2832 (2010).
24. Y. Julien and J. A. Sobrino, "Comparison of cloud-reconstruction methods for time series of composite NDVI data," *Remote Sens. Environ.* **114**(3), 618–625 (2010).

25. B. N. Holben, "Characteristics of maximum-value composite images from temporal AVHRR data," *Int. J. Remote Sens.* **7**(11), 1417–1434 (1986).
26. N. Viovy, O. Arino, and A. S. Belward, "The best index slope extraction (BISE): a method for reducing noise in NDVI time-series," *Int. J. Remote Sens.* **13**(8), 1585–1590 (1992).
27. D. Krstajic et al., "Cross-validation pitfalls when selecting and assessing regression and classification models," *J. Cheminf.* **6**(1), 1–15 (2014).
28. B. G. Marcot and A. M. Hanea, "What is an optimal value of k in k-fold cross-validation in discrete Bayesian network analysis?" *Comput. Stat.* **36**(3), 2009–2031 (2021).
29. K. G. Russell and G. Congalton, *Assessing the Accuracy of Remotely Sensed Data Principles and Practices*, CRC Press (1999).
30. C. S. Ministry of Economy, Trade and Industry, "Regional economy society analyzing system," https://resas.go.jp/ (accessed 22 July 2020).
31. Japan Meteorological Agency, "Annual meteorological data in 2018 in Tsuchiura city, Japan," (2018). https://www.data.jma.go.jp/obd/stats/etrn/view/annually_a.php?prec_no=40&block_no=0324&year=2018&month=&day=&view= (accessed 17 December 2020).
32. Ministry of Agriculture, Forestry and Fisheries, "Statistical survey on crops" (2018). https://www.e-stat.go.jp/stat-search/files?page=1&layout=datalist&toukei=00500215&tstat=000001013427&cycle=7&year=20180&month=0&tclass1=000001033085&tclass2=000001125855&tclass3val=0 (accessed 22 July 2020).
33. Ministry of Agriculture, Forestry and Fisheries, "Graphs and statistics on agriculture, forestry, and fisheries (Ami-town, Japan)," (2015). http://www.machimura.maff.go.jp/machi/contents/08/443/index.html (accessed 19 July 2019).
34. Planet.com, "Planet imagery product specifications August 2019," (2019). https://assets.planet.com/docs/combined-imagery-product-spec-final-august-2019.pdf (accessed 8 January 2020).
35. D. Scheffler et al., "AROSICS: an automated and robust open-source image co-registration software for multi-sensor satellite data," *Remote Sens.-Basel* **9**(7), 676 (2017).
36. National Chamber of Agriculture, "Agricultural land information system agricultural committee," https://www.alis-ac.jp/ (accessed 11 August 2020).
37. A. A. Nielsen and K. Conradsen, "Multivariate alteration detection (MAD) and MAF post-processing in multispectral, bitemporal image data: new approaches to change detection studies," *Remote Sens. Environ.* **64**(1), 1–19 (1998).

Yoshihiko Kobayashi received his BAgr and MAgr degrees from the Ibaraki University in 2019 and 2021, respectively. Currently, he is working as a researcher at the National Agriculture and Food Research Organization in Japan. His research interests include GIS and prevention of agricultural accidents.

Tsuguki Kinoshita received his PhD degree in engineering from the University of Tokyo in 1999. Currently, he is working as a professor at Ibaraki University. He is the author of more than 30 journal papers. His research interests include land-use change, climate change, forecast, and GIS.